INL/EXT-20-59941

Light Water Reactor Sustainability Program

Assessment of Grizzly Capabilities for Reactor Pressure Vessels and Reinforced Concrete Structures

Benjamin W. Spencer
William M. Hoffman
Sudipta Biswas
Amit Jain

September 2020

DOE Office of Nuclear Energy

INL/EXT-20-59941

Light Water Reactor Sustainability Program

Assessment of Grizzly Capabilities for Reactor Pressure Vessels and Reinforced Concrete Structures

Benjamin W. Spencer
William M. Hoffman
Sudipta Biswas
Amit Jain

Idaho National Laboratory

September 2020

Idaho National Laboratory
Idaho Falls, Idaho 83415

http://www.inl.gov/lwrs

Prepared for the
U.S. Department of Energy
Office of Nuclear Energy
Under DOE Idaho Operations Office
Contract DE-AC07-05ID14517

ABSTRACT

Over the last several years, capabilities to simulate the progression and effects of degradation in critical structures in light water reactor (LWR) nuclear power plants have been under development in the Grizzly code. Age-related material degradation is important for a number of systems in LWRs, but the main focus for Grizzly development has been on reactor pressure vessels (RPVs) and concrete structures because of their central role and the difficulty of replacement of these structures if they are found to be degraded to an unacceptable degree.

The capabilities for analyzing both RPVs and concrete structures in Grizzly have reached a point where the feature sets are sufficiently complete to perform credible analyses of those types of structures. Because of this, the emphasis has shifted from foundational development to assessing the accuracy of these modeling capabilities on representative problems of interest and on improving the physical basis of those models to improve their ability to predict the actual response of those structural systems.

This report documents a first set of test cases that have been developed to assess the Grizzly code on real-world problems for these two types of structures. For RPVs, these test cases consist of a set of benchmark problems where Grizzly is compared to another code. For concrete structures, a set of models of experimental specimens designed to characterize the multidimensional swelling response of reinforced concrete members due to alkali-silica reaction (ASR) has been developed and compared with experimental results.

Both the RPV and concrete test cases developed here are much more computationally intensive than the small regression tests that are used in the testing that Grizzly undergoes every time a proposed set of changes is made to ensure that those changes do not adversely affect previously established behavior. A system for regularly running these large problems to monitor the behavior of the code as it is developed has been instituted. While these test cases generally indicate good comparison with the benchmark results, they also indicate areas where further development is warranted.

CONTENTS

FIGURES

ACRONYMS

ASR	alkali-silica reaction
ASME	American Society of Mechanical Engineers
ASTM	American Society for Testing and Materials
CFD	computational fluid dynamics
CPF	conditional probability of failure
CPI	conditional probability of fracture initiation
DOE	Department of Energy
EMDA	expanded materials degradation assessment
INL	Idaho National Laboratory
LWR	light water reactor
LWRS	Light Water Reactor Sustainability
ODE	ordinary differential equation
PTS	pressurized thermal shock
PFM	probabilistic fracture mechanics
PWR	pressurized water reactor
RIVE	radiation-induced volumetric expansion
RPV	reactor pressure vessel
SQA	software quality assurance
XFEM	extended finite element method

1 Introduction

The current set of operating light water reactor (LWR) nuclear power plants provides a critical source of clean base energy generation. The capital costs and time required to construct such plants are high, so safely maintaining the continued operation of these plants is essential. The materials that comprise the safety-critical structures in these reactors are subjected to harsh operating conditions and degrade over time. Grizzly is a simulation code being developed at Idaho National Laboratory (INL) to simulate the progression of aging in key structural components in nuclear power plants. Although Grizzly's scope has broadened in recent years to include advanced reactors, original development of Grizzly was solely focused on LWRs and funded by the U.S. Department of Energy's (DOE's) Light Water Reactor Sustainability (LWRS) program.

Grizzly development for LWR applications has focused on two main structural systems: reactor pressure vessels (RPVs) and concrete structures. Both types of structures have critical safety roles and would be extremely costly and impractical to replace if it were found that they had degraded to an unacceptable degree. Both were also identified as having high importance by the expanded materials degradation assessment (EMDA) evaluation [1, 2].

Recent work on Grizzly has focused on filling gaps in capabilities in the areas of RPV and reinforced concrete structure analysis [3]. While these capabilities are still under development, they are sufficiently feature complete to begin applying them to engineering analyses and it is important to assess their performance and accuracy on relevant problems. This report documents the development of a set of test cases to assess Grizzly on larger-scale problems for these two types of structures.

Grizzly development adheres to a set of software quality assurance (SQA) procedures that include revision control, peer review, documentation, and testing for all changes made to the code base. Grizzly has a growing suite of regression tests that are small, fast-running problems that ensure that changes to the code do not adversely affect accepted code behavior. There is also a need for test cases that ensure that the code adequately performs on larger problems relevant to code users. A suite of larger test cases that is automatically run on a regular basis has been established, as described in Section 2.

As RPVs are exposed to the service environment that consists of elevated temperatures and a high neutron flux from the reactor core, their steel becomes increasingly brittle. During a transient event, the flaws introduced during manufacturing are potentially subjected to a combination of elevated stresses and decreased temperatures, which applied together can lead to fracture initiation, and potentially failure of the RPV. An important engineering metric is the probability of fracture of any flaw in the population during a transient event, which is computed using a procedure known as probabilistic fracture mechanics (PFM). The fracture mechanics solutions can be verified against analytic solutions, and have been to some extent. Because of the nature of this problem, it is difficult to validate the PFM model against analytic solutions. Although it is not sufficient to guarantee accuracy, benchmarking against another code can instill some level of confidence in a code, and that is done here for the PFM models in Grizzly, as described in Section 3.

Concrete structures are subjected to environmental conditions that can lead to degradation through multiple mechanisms. Most of these mechanisms are common to all civil structures, and many of them involve a combination of thermal, moisture, and chemical species transport, coupled with mechanical deformation. The foundational models for multiple degradation mechanisms that provided by Grizzly are implemented in an open-source code called BlackBear, which provides structural degradation models that are not specific to nuclear applications. Grizzly provides all of the capabilities of BlackBear, as well as a model for radiation-induced volumetric expansion (RIVE), which is applicable to irradiated concrete in the vicinity of a nuclear reactor. Development of concrete capabilities in Grizzly/BlackBear has primarily focused on RIVE and alkali-silica reaction (ASR), which is an expansive reaction between alkali in the hardened cement paste and aggregates with high silica content. This expansion, which generally occurs over long periods of time, can cause functional problems and cracking in the concrete, and is an issue of current concern in at least one operating LWR. The testing of the concrete capabilities documented here focused on ASR, and

compare predicted response with experimental results for a number of reinforced concrete specimens subjected to accelerated ASR in a laboratory environment. These tests, described in Section 4, exercise multiple capabilities in Grizzly/BlackBear, including models for ASR expansion, creep, and reinforcing steel.

2 Automated Nightly Testing

The set of SQA procedures followed in Grizzly development require testing for all changes made to the code base to ensure that they do not adversely affect accepted code behavior. Grizzly and BlackBear both have extensive and growing suites of test problems that are developed for this purpose. These tests exercise both individual components of the code in isolation, as well as combinations of features, and are extremely important for ensuring code quality. However, these tests are designed to be fast running (on the order of 2 seconds or less), and thus are limited in their ability to replicate the usage of the code on large-scale problems of interest.

As part of the present work documented here, a set of larger test cases more representative of those a user would run for engineering simulations of interest has been established. The structure of these test problems in the Grizzly and BlackBear source code directories mimics that of the BISON code [4], and is contained in two main subdirectories at the top level of these code repositories: `examples` and `assessment`.

- The `examples` directory (which is currently only populated for Grizzly), contains input files for simulations representative of those that a user might run in practice. These simulations do not necessarily have benchmark results for comparison, but are useful for illustrating the process of setting up a model.
- The `assessment` directory contains input files for simulations that can be compared against benchmark results. These can be characterized as verification cases (where there are comparisons with analytical solutions), validation cases (comparisons with experimental results), or benchmarking (comparisons with solutions from other codes).

Because some of these models require extensive computational resources, it is not practical to run them for every code change. However, all of the input files are checked to ensure that they have valid, up-to-date syntax for every code change, and all models are run by an automated process that executes them on a regular basis (nightly for the smaller cases, and weekly for the larger cases). Selected results from these simulations are automatically checked against accepted solutions every time they are run, and a report on the status of the tests is sent out to the code developers so that if issues are identified with any of these tests, they can be corrected quickly. The same system (the `run_tests` script provided by the MOOSE system that Grizzly is built on) that is used to run the regression tests is used to run these larger test cases.

Currently, the Grizzly "example" problems consist of a set of models that compute the thermal/mechanical response of a prototypical RPV under transient loading conditions. These models all represent the same RPV and transient conditions, but with varying dimensionality:

- 1D axisymmetric
- 2D axisymmetric, with a single strip of elements
- 2D planar (cross-section of the RPV in a plane normal to the axis of rotation)
- 3D quarter symmetry of a cylinder (beltline region only)
- 3D quarter symmetry model of full vessel.

Figure 1 shows representative responses of some of these models, and illustrates how the lower-dimensional models can represent the behavior of the beltline region of the RPV, where the material is sufficiently distant from geometric features that the response of the RPV can be idealized as that of a cylinder of infinite height.

The Grizzly "assessment" cases consist of PFM models that evaluate the probability of failure of the beltline regions of RPVs with full populations of flaws representative of those that might be found in an actual

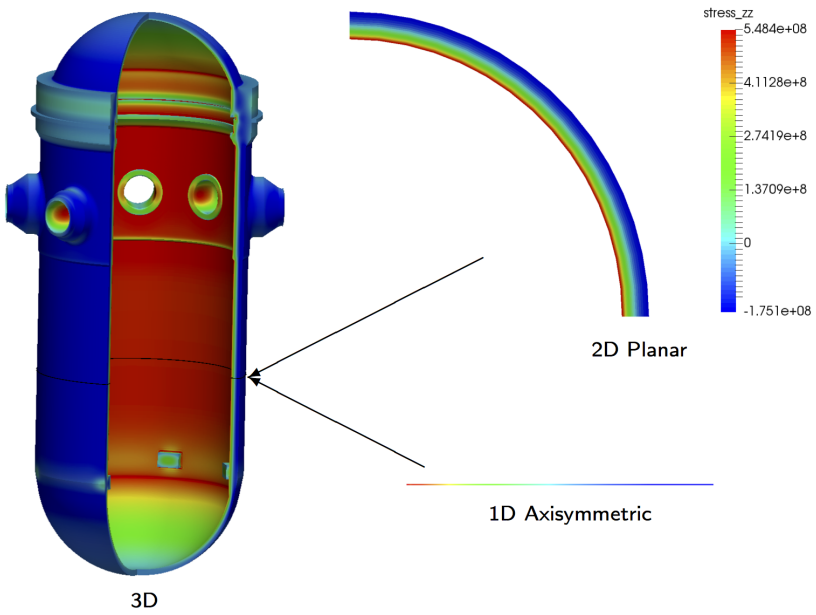

Figure 1. Representative results of some of the RPV models in the Grizzly "examples" test suite, showing 1D axisymmetric, 2D planar, and 3D Grizzly models of the global response of a PWR RPV at a point in time during a PTS event. 1D and 2D models represent the response on the plane in the beltline region shown by the dark line in the 3D model, and match the behavior of the 3D model on that plane [5].

RPV. These models are based on the response of an infinite cylindrical idealization of the RPV, modeled using the 1D model in the "examples" directory. These models are described in Section 3 of this report, and are being expanded as more cases are developed.

The BlackBear "assessment" cases currently consist of a subset of the ASR simulations described in Section 4 of this report. These cases are considered validation problems because they compare simulations against experimental data. At this point, these models consist of relatively small concrete block problems, but the BlackBear "assessment" and "example" problems will be expanded over time to include larger models of structures more representative of those of interest for engineering applications.

3 Engineering-Scale Reactor Pressure Vessel Benchmarking

Computing the probability of failure of an RPV under a transient event consists first of analyzing the global thermo/mechanical response of the RPV, followed by a PFM calculation, where the likelihood of failure using random realizations of the flaw is computed using outputs from the thermo/mechanical analysis. Both stages of this analysis must be performed correctly for accurate results. It has been shown previously that Grizzly is capable of accurately measuring the thermomechanical response of a reactor pressure vessel (RPV) during various types of transient events [5], so the focus here is primarily on benchmarking the PFM stage of the analysis. The details of the global thermo/mechanical analysis that forms the basis for the PFM benchmarks are first outlined here, followed by the details of the PFM analysis.

3.1 Global RPV Models

Simulations of the global response of the beltline region of the RPV can be performed using models of varying dimensionality, as dictated by the conditions to be considered. The temperature and pressure boundary conditions shown in Figure 2 were used in all cases considered here, and are taken from a realistic pressurized thermal shock (PTS) scenario in the test cases of the FAVOR code [6]. This transient is particularly aggressive, and represents a scenario in which a pressure release valve is stuck open, resulting in depressurization and significant decrease in temperature, followed by a rapid repressurization and slow temperature increase once the valve closes again. Corresponding to this transient, a temperature dependent heat transfer coefficient history taken from the same source as the pressure and temperature history was used for the convective flux boundary condition applied at the inner surface of the RPV.

When these conditions were applied uniformly to the interior of the RPV, the 1D, 2D, and 3D models were shown to produce similar results in a prior study [5] in the beltline region, as shown in Figure 1. In that study, fracture mechanics solutions for flaws evaluated using the stresses from the models of varying dimensionality were demonstrated to produce equivalent histories of the mode-I stress intensity factor, K_I, during the transient event, as shown in Figure 3. The 1D model can be used for simplicity and speed, but if non-uniform spatial boundary conditions are being applied (e.g., to capture thermal streaming effects), a

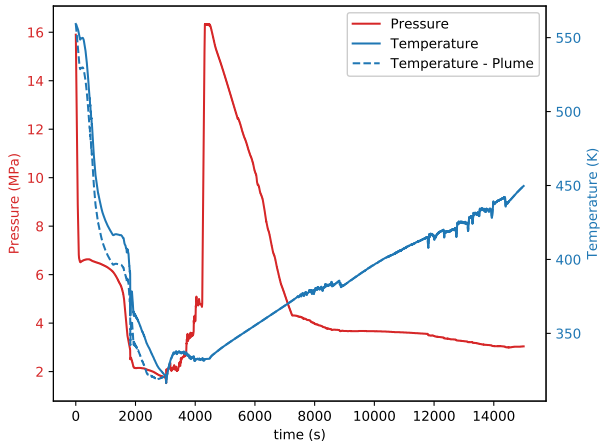

Figure 2. Internal pressure and temperature loading histories used for RPV analyses. A single pressure history is applied uniformly in all cases. Two temperature histories are shown – one applied to the whole vessel in most cases, as well as a more rapidly decreasing temperature history applied for a special case where plume effects were considered [5].

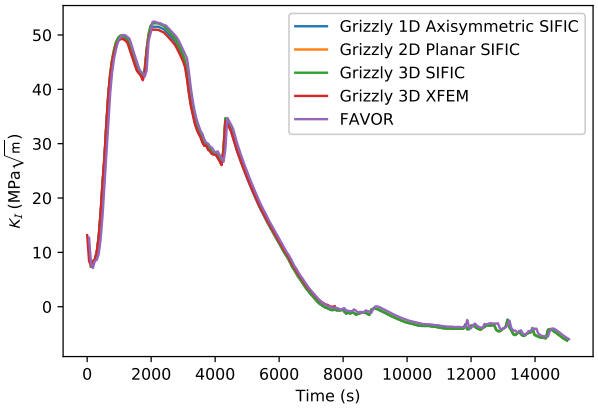

Figure 3. Comparison of time history of K_I during the representative PTS transient shown in Figure 2 for an axis-aligned circumferential surface-breaking flaw in the RPV shown in Figure 1. Grizzly SIFIC results use through-wall stress solutions computed from 1D, 2D, and 3D Grizzly global RPV models. These are compared with results from a 3D Grizzly XFEM model and a FAVOR model of the same flaw. From [5].

more detailed 3D model is necessary and can be used by Grizzly.

The RPV geometry and dimensions used here are based on publicly available information on a typical four-loop PWR pressure vessel, but do not represent a specific RPV. The RPV used in this study has internal radius of 2.1971 m, a cladding thickness of 0.004064 meters, and a base-metal wall thickness of 0.219202 meters. Temperature-dependent material properties for the base metal and stainless steel liner were used for the base metal and cladding materials, respectively.

3.2 RPV PFM models

Because prior work has established the adequacy of the global response and deterministic fracture mechanics models, the primary objective of the present study was to benchmark Grizzly's PFM capabilities against those of another code. Grizzly's PFM algorithms are based on those of FAVOR. Grizzly builds on the capabilities in FAVOR, providing additional features such as multidimensional (1D, 2D, or 3D) modeling, parallel computing, a more flexible and modern framework, the ability to evaluate off-axis flaws. For an equivalent problem based on a 1D assumption of the global RPV response, the two codes should produce very similar results.

For this benchmarking study a number of probabilistic fracture mechanics (PFM) simulations were run using both Grizzly and FAVOR. All cases are based on the same global RPV characteristics, but evaluate different configurations of the region of the RPV where flaws are evaluated. The beltline region of the RPV is usually of the most concern because it is subjected to the highest irradiation, and depending on the construction of the RPV, can consist of multiple forgings or plates welded together. Each of these types of regions is treated differently in the PFM analysis.

The simplest test cases consist of analyses of the populations of flaws in simple regions: a single plate region, a single forging region and a single weld region. These types of regions are not representative of an entire vessel, but it is important to benchmark their behavior before moving to more complex configurations. Further analysis was then done using more representative groupings of regions that comprise the entire beltline region. One model consists of six plates which are joined together by seven weld regions, and the other consists of two forgings joined together by a single circumferential weld. These models are all illustrated in Figure 4.

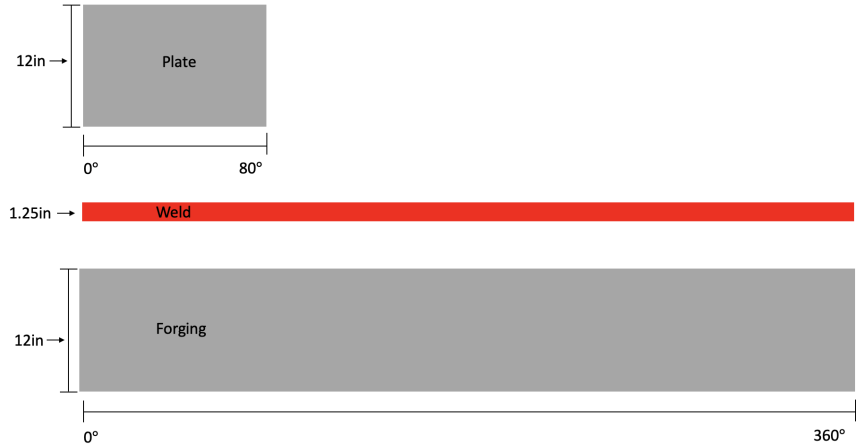

(a) Individual component models

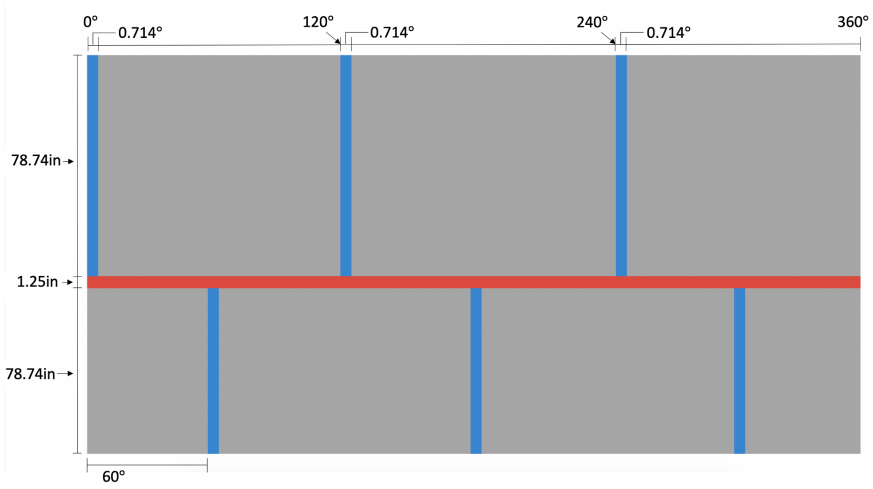

(b) Full beltline region of RPV composed of plates and welds

(c) Full beltline region of RPV consisting of forgings and weld

Figure 4. Configurations of RPV in beltline region considered in benchmark PFM analyses

The PFM models in Grizzly and in FAVOR require a number of material properties to be defined for the various types of RPV regions being simulated. The properties used for benchmarking of the individual RPV regions, (single plate, forging, weld models), are listed in Table 1. The initial nil-ductility reference temperature (RT_{NDT}) has a strong effect on the likelihood of failure and can vary significantly. Higher values of this parameter correspond to higher likelihoods of failure. In models with weld regions, the welds often have higher densities of flaws that are more likely to fail. For the two models of the full beltline region containing multiple plates and welds, and multiple forgings joined by a single weld, RT_{NDT} for the weld region was reduced to -50°F so that the weld region would not dominate the response of the entire model.

Table 1. Mean values of key material properties used for the region types in demonstration RPV simulations.

Material	**Surface Fluence** (10^{19} **n/cm**^{2})	**Cu** (**wt%**)	**Ni** (**wt%**)	**Mn** (**wt%**)	**P** (**wt%**)	**Initial RT**$_{NDT}$ (**°F**)
Plate	6.0	0.2	0.6	1.3	0.01	50
Forging	6.0	0.2	0.6	1.3	0.01	50
Weld	4.0	0.258	0.165	1.44	0.017	50

The primary metric of interest in a PFM calculation is the probability of crack initiation, conditional on occurrence of a given transient. This conditional probability of initiation (CPI) is computed by performing Monte Carlo analysis using a large number of random realizations of flaw populations. The distributions of flaw densities are separately prescribed for embedded flaws in plates and welds using data from [7]. Surface-breaking flaws tend to be more likely to be initiation sites for fracture because the inner surface experiences the highest embrittlement.

Because representative experimentally-characterized date for surface-breaking flaw distributions were not available, contrived distributions that exercised a variety of flaw depths were developed for this study. Surface-breaking flaws are prescribed with an arbitrary uniform density of 0.00465 flaws/m^2 and flaw depths reaching beyond the cladding to 2 3 and 4% of the total wall thickness were considered. Of those flaws, 80% have an aspect ratio of 2, 15% have an aspect ratio of 6, 4% have an aspect ratio of 10 and 1% have an infinite aspect ratio. The characterization of this flaw density is not representative of real flaw data, but was chosen only for demonstration purposes.

The probabilities computed in PFM analyses can vary by orders of magnitude depending on the types of flaws considered; so to independently ensure that the models for surface-breaking and embedded flaws are behaving correctly, it is important to consider the populations of the separate types of flaws independently. Thus PFM computations were performed for cases with only embedded flaws, only surface-breaking flaws, and for both types of flaws together.

Residual stresses induced in the welding process can be considered in PFM analyses performed by Grizzly. The FAVOR methodology [8] for applying residual stress to heat-affected zones is adopted by Grizzly, as described in [3]. Residual stress data was collected for use within the FAVOR code, shown by the black dots in Figure 5. In Grizzly, the data is captured using a fourth order polynomial for surface breaking flaws, and an eighth order polynomial for embedded flaws. Due to the design of the reduced order model for surface breaking flaws, Grizzly is limited to the use of a fourth order polynomial. It is clear from Figure 5 that a fourth order polynomial does not adequately capture the details of the through wall stress distribution over the entire thickness of the wall. The current work-around for this is to fit the polynomial over just the length of the deepest reaching surface breaking flaw. A fourth order polynomial is sufficient for capturing the details of that particular stress profile up to approximately 1/4 of the vessel wall. A more robust and accurate method for implementing weld residual stresses in surface breaking flaws should be considered and implemented in the future. PFM calculations are performed here both with and without residual stresses for the single weld

case.

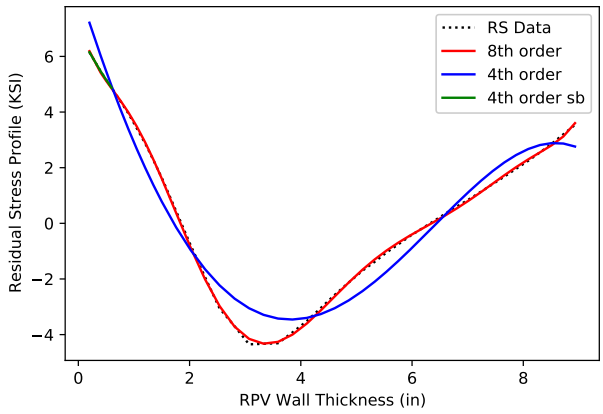

Figure 5. Through-wall variation of the residual stress, including experimental data and polynomials used to describe the residual stress through the wall of the vessel in Grizzly.

Because there can be significant variation in the computed CPI from one RPV realization to the next, it is important to perform a sufficient number of samples until the Monte Carlo iterations are converged. To illustrate convergence of the Monte Carlo iterations, the history of the CPI over the course of these iterations are shown for each of these cases for the Grizzly model. The history of the CPI value is not important to the final outcome; however, plotting it illustrates that convergence has been achieved. The average CPI varies significantly early in the iterations but should be flat over a large number of iterations for convergence. As shown in the following plots, the same number of RPV realizations (1,000,000) is used in all cases, and is sufficient for adequate problem convergence. The convergence histories of Grizzly and FAVOR show similar characteristics, but to avoid unnecessary complexity, only the history for Grizzly is shown here.

Figure 6 shows the history of convergence of CPI for the PFM models with only embedded flaws, while Figure 7 shows equivalent convergence histories for the same cases with only surface-breaking flaws and Figure 8 shows the same quantities for combined surface-breaking and embedded flaw scenarios.

Currently in Grizzly there is not a way to apply the two different types of residual stress polynomials in a single analysis containing both surface breaking and embedded flaws. Grizzly can in theory be run using a fourth order approximation of the residual stress over the entire depth of the RPV wall for both surface breaking and embedded flaws, but this method is not accurate and grossly misrepresents the effect of the residual stresses. More development work is required in order to address this shortcoming. Additionally more work is required to allow Grizzly to run PFM analyses considering the effects of residual stresses containing multiple regions, only some of which may be affected by residual stresses. Because of this, comparisons were not shown with residual stresses for a combination of embedded and surface-breaking flaws.

The following observations can be made from these results:

- Overall, the comparisons between Grizzly and FAVOR are quite good. If algorithms were implemented identically, one would expect that the Monte Carlo simulations would eventually converge to the same results for the two codes. Although the same algorithms were generally adopted in the two codes, there are some cases in Grizzly where different modeling choices were made for a number of reasons.

- There are still areas where differences between the codes are significant enough to warrant further investigation. In particular, the models with a single weld region, as well as the forgings and weld models deserve further attention.

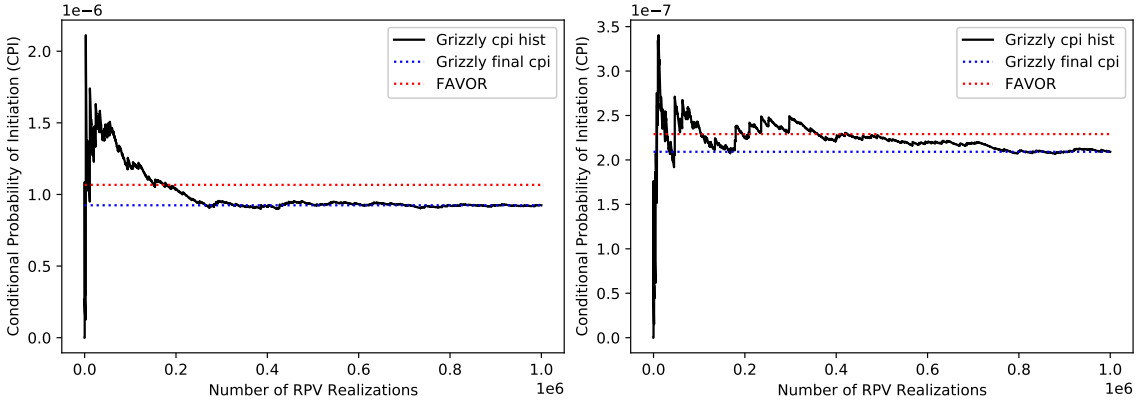

(a) Single plate

(b) Single forging

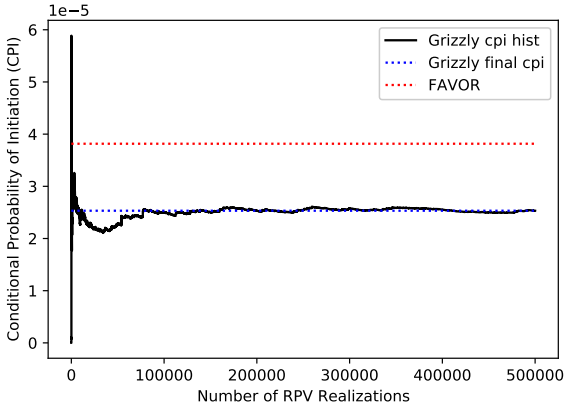

(c) Single weld

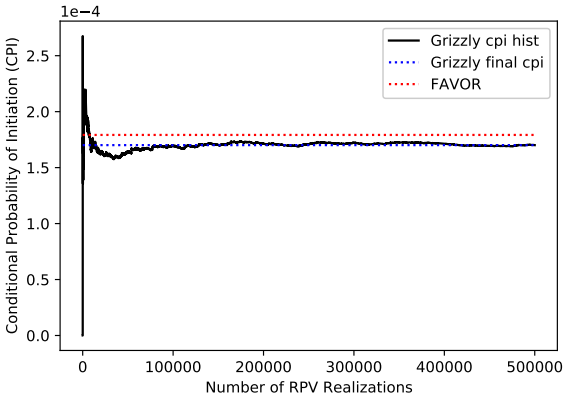

(d) Single weld with residual stress

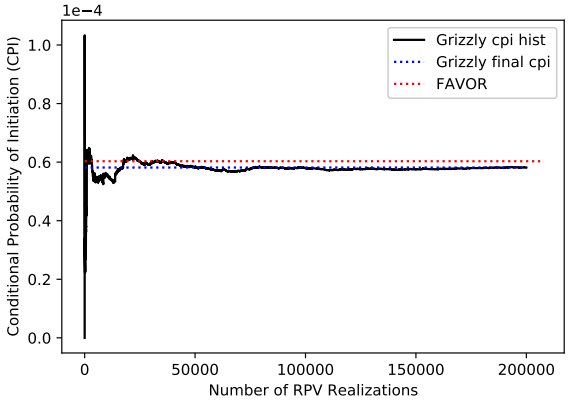

(e) Plates and welds

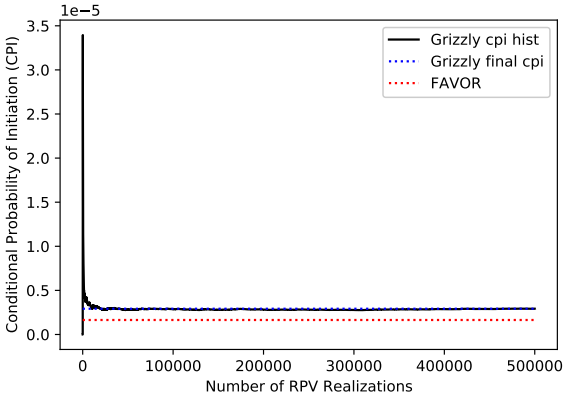

(f) Forgings and weld

Figure 6. CPI convergence history for PFM models with embedded flaws only

Ongoing and future development of Grizzly will change its behavior and push it farther from that of FAVOR. For example, improved models for calculation of K_I for embedded flaws that have reduced conservatism have recently been developed for Grizzly, and will be deployed after further testing. It is expected that use of these models may significantly decrease the computed CPI in some cases. The present work of establishing that the baseline algorithms are implemented correctly is important before moving forward with such new development.

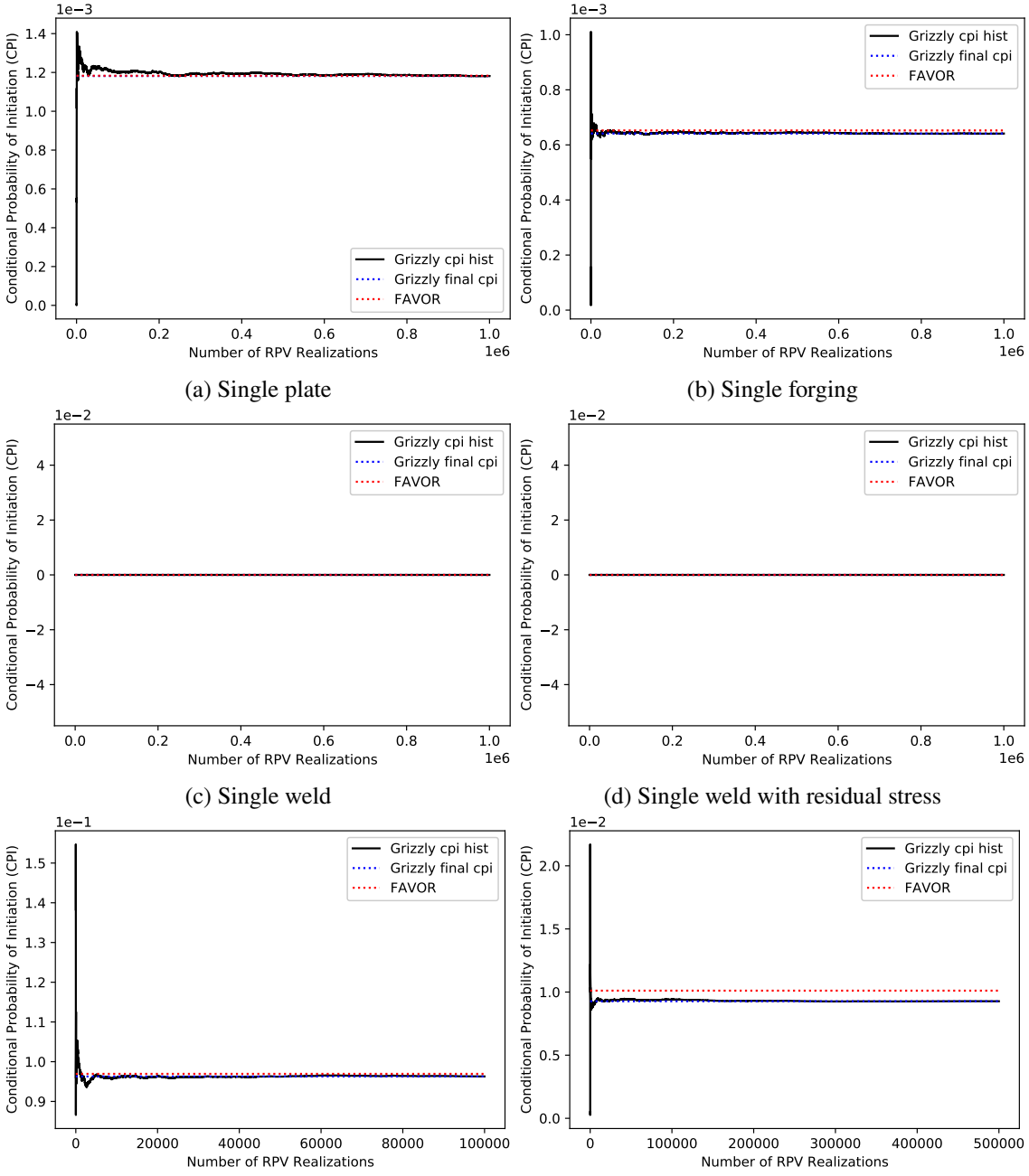

(a) Single plate

(b) Single forging

(c) Single weld

(d) Single weld with residual stress

(e) Plates and welds

(f) Forgings and weld

Figure 7. CPI convergence history for PFM models with surface-breaking flaws only

3.3 Initiation, growth, and arrest model testing

One area of recent development in Grizzly was the implementation of a model for initiation, growth, and arrest of cracks. This is an extension to the PFM model that uses further probabilistic sampling to compute the likelihood of a crack that has initiated propagating through the wall of an RPV. The result of this is a conditional probability of failure (CPF), which is a number between 0 and CPI for a given PFM analysis, and which is an alternative, but less-conservative metric of RPV safety during a given transient. Development of a preliminary version of this model was performed in the prior year [3]. Testing is currently underway

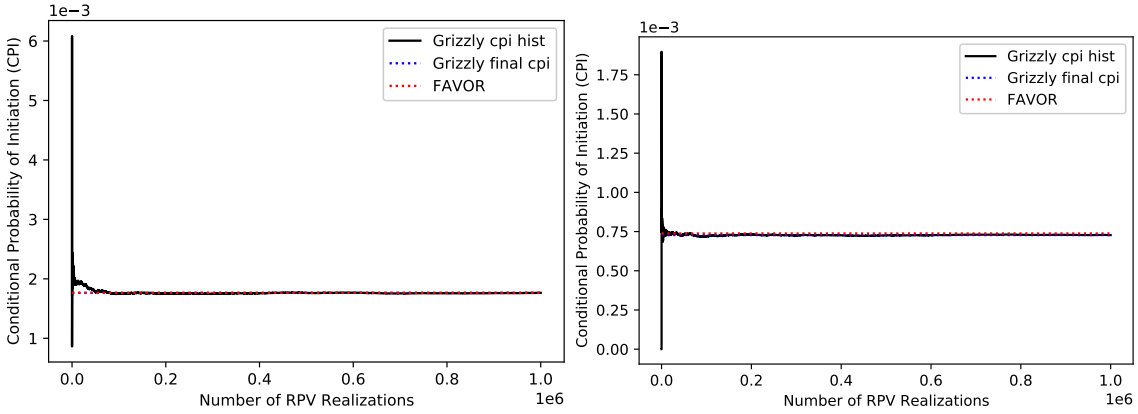

(a) Single plate

(b) Single forging

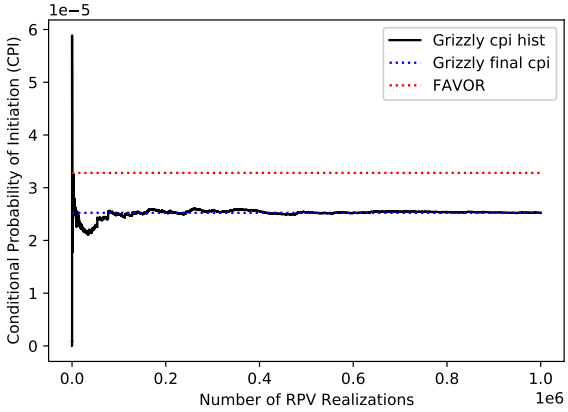

(c) Single weld

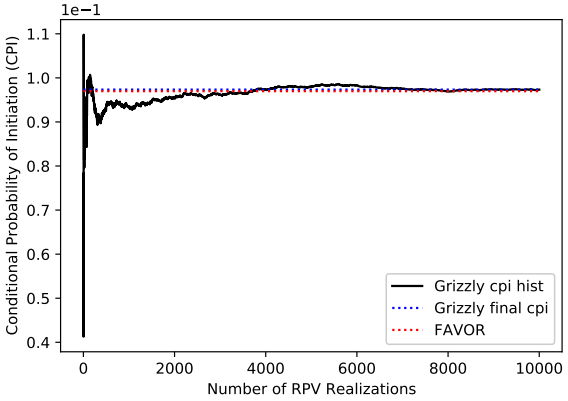

(d) Plates and welds

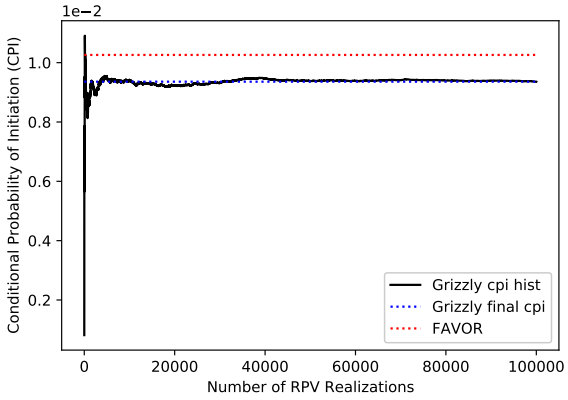

(e) Forgings and weld

Figure 8. CPI convergence history for PFM models with both surface-breaking and embedded flaws

on this model using the same benchmark cases described for CPI calculation, but the agreement between the FAVOR and Grizzly results is still inadequate. These benchmark cases are very useful for testing of this model, and once adequate agreement is reached, this model will be fully merged into Grizzly.

Figure 9. Quarter-symmetry 3D RPV model used in this demonstration. Temperature contours at a point in time during the rapid cooling phase are shown to identify the region where the cold plume was applied (shown in blue).

3.4 Plume analysis demonstration

The work documented here is primarily focused on comparing Grizzly PFM simulations against benchmark cases based on 1D models of global response. However, it is important to emphasize that the goal of Grizzly development is not simply to match the capabilities of an existing code, but to enable the consideration of important physical phenomena that cannot be considered with currently available tools. This is possible once these benchmarking simulations have been performed.

One important phenomenon that requires a multi-dimensional PFM code is the analysis of the effects of spatially non-uniform cooling. The 1D simulations shown in this report all assume that when an RPV is flooded with lower-temperature coolant during an accident, the coolant has a uniform temperature everywhere in the RPV, which is a simplification of actual conditions. A simplified, proof-of-concept demonstration of consideration of the effects of non-uniform cooling in a PFM calculation is shown here.

To idealize the nonuniform temperature conditions, a plume region emanating downward from an inlet is identified on the RPV model as shown in Figure 9. The same transient temperature and pressure history applied previously in the 1D PTS analyses assuming spatially uniform conditions is used as the basis for the transient applied here, and is applied to the balance of the inner surface of the RPV, while a more rapidly decreasing temperature function is used in the plume region. As can be seen in Figure 9, there is a region between the plume and non-plume regions over which the temperature linearly transitions between the two functions.

The plume temperature history was created as an offset to the non-plume baseline function shown in Figure 2 such that the maximum temperature difference between the plume and non-plume region is 20 °C. The plume function drops the temperature more quickly than the non-plume region for the first 3000 seconds until it reaches the same temperature as the rest of the inner surface, and then the functions are the same.

It is important to emphasize that this is a contrived example created to demonstrate this capability in Grizzly. The shape and size of the plume region, as well as and the temperature difference between the plume and non-plume region, are approximations and do not represent actual expected conditions. High fidelity computational fluid dynamics (CFD) simulations could be used to compute more realistic transient coolant-temperature distributions.

Appropriate symmetry conditions were applied to the model shown in Figure 9 to allow it to the response of the full RPV, assuming that all inlets experience the same plume effects.

To quantify the effect of the plume, two versions of the model were run: one with separate temperature histories applied to the plume and non-plume regions, and a baseline case in which the non-plume baseline temperature history is applied everywhere in the inner surface of the RPV. The heat-transfer coefficient in general varies spatially and temporally over the course of the transient, but because a full CFD analysis would be required to establish this for a spatially varying temperature, a constant value of 5000 W/(m^2K) was used throughout the analysis.

Figure 10 shows the spatial distribution of flaws with nonzero CPI after 1,000,000 Monte Carlo iterations superimposed on the temperature distribution at one point in time during the transient. This does not indicate that all of these flaws exist in a given RPV, but regions with high density of these flaws indicate where failure is more likely. This simulation clearly indicates a higher likelihood of failure in the plume region, where more rapid cooling leads to lower steel temperatures and higher thermally induced stresses. This is only a proof-of-concept demonstration, and as previously mentioned, 3D CFD simulations would be necessary to provide realistic boundary conditions, but this shows the potential of the multidimensional PFM capabilities in Grizzly.

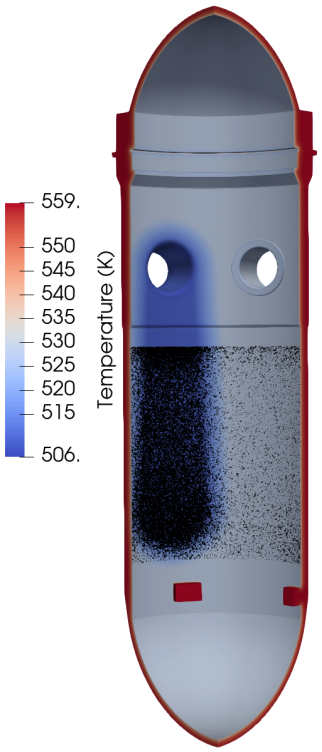

Figure 10. Locations of flaws with nonzero CPI over 1×10^6 Monte Carlo iterations superimposed on the RPV global model, superimposed on the temperature field at one point during the cool-down phase of the transient.

4 Validation of Alkali-Silica Reaction in Concrete

Development of a set of tests to validate the concrete models in BlackBear against experimental data is currently underway. Multiple experimental studies provide data adequate for validation of the ASR models in BlackBear, and as documented here, several validation cases have been developed based on some of these studies. These include experiments on relatively simple blocks with reinforcement, as well as more complex beams, which are more representative of actual structures of interest.

4.1 Concrete Block Cases

Wald et al. [9] performed a series of experiments to understand how the presence of multiaxial reinforcement affects ASR expansion behavior of concrete. In their study, a set of 33 reinforced concrete cubes with side lengths of 480 mm and varying reinforcement configurations were exposed to environmental temperature and humidity, while monitoring multiaxial expansion. Four unreinforced specimens were monitored to obtain the free expansion behavior of the concrete. These experiments are well-suited to assess the ability of the rebar models in BlackBear to predict the confining effect of rebar on concrete structures affected by ASR.

Some of these experiments are modeled here including an unreinforced block (Specimen A1-000b), and several blocks with varying reinforcement configurations. Figure 11 shows the BlackBear model of these blocks with rebar modeled as 1D trusses. This shows the configuration of the reinforcement bars oriented in the x-, y- and z-directions distributed in two or three layers. The details about various rebar configuration models used in this analysis are provided in Table 2. Here, the specimen nomenclature follows the naming convention of Ref [9]. The concrete is modeled with a uniform $32 \times 32 \times 32$ mesh of linear hexahedral elements, while each rebar is meshed with 23 elements along its axial dimension. As can be seen from this image, the nodes of the rebar mesh do not coincide with nodes of the concrete mesh in most cases. Constraints are used to tie the nodes of the rebar to the concrete elements. The model of the unreinforced block is not shown here, but is identical to the models shown, except for the absence of rebar.

The BlackBear models of these blocks solved for temperature, relative humidity, and displacement fields using the models described in our recent publication [10]. The mechanical model included ASR expansion and creep in the concrete. Table 3 shows the material properties used in the BlackBear models. The only mechanical boundary conditions applied to the blocks were pinned constraints to prevent rigid body motion, but to allow unrestrained free expansion. For thermal and humidity boundary conditions, experimental temperature and humidity histories [9], as shown in Figure 12, are applied on all outside boundaries of the concrete blocks.

In the simulations, the average temperature response of the block closely follows the environmental temperature prescribed on the boundaries of the block because heat conduction occurs rapidly relative to the time scale of the experiment. However, due to the low permeability of the concrete, moisture transport occurs over much longer time scales, and the average value of the relative humidity can differ significantly from the value at the boundary, as shown in Figure 12, which compares the computed average temperature and relative humidity in the concrete block with the values applied at the boundaries.

During the experiments, the axial expansion in three directions was monitored. These measurements include all sources of expansion, which include ASR and thermal expansion. Since data for ASR expansion in isolation are not available, the parameters that control the ASR expansion model were calibrated to match the average axial expansion reported in the plain concrete block. The displacement values were extracted from the simulation at the same six points, which were considered during the experiments [9], on each of the surfaces. The average expansion here represents the average of measurements from these six points. Considering the curing time of 28 days, the simulations were started at 28 days except otherwise mentioned. Figure 13 shows the experimental and simulation results, which indicate that, with calibration, the model is able to to replicate the experimentally observed behavior reasonably well.

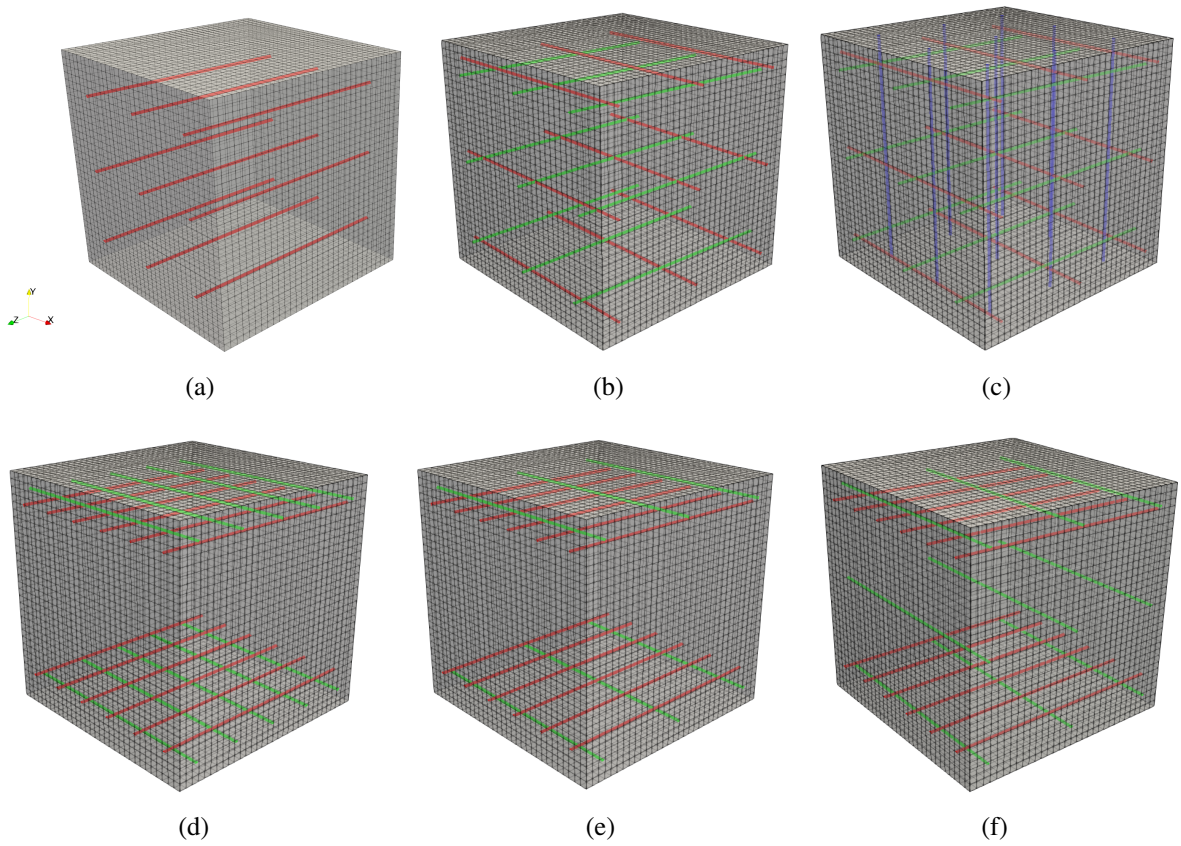

Figure 11. BlackBear model of concrete block with various reinforcement configurations: (a) Uniaxial, (b) Biaxial, (c) Triaxial, (d) Biaxial-L1, (e) Biaxial-L2, (f) Biaxial-L3.

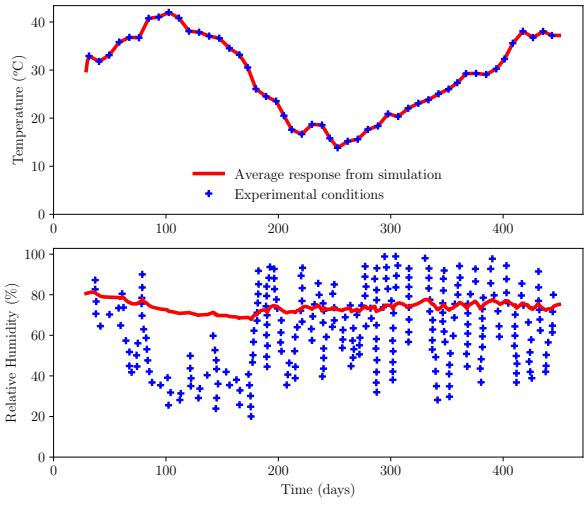

Figure 12. Time history of temperature (top) and relative humidity (bottom), including reported values from experiments [9] applied to the boundary of the BlackBear model, along with average values computed in the plain and reinforced blocks in the BlackBear models.

Table 2. Details of the concrete block specimens.

Reinforcement Arrangement	**Specimen Name**	**Reinforcement Fraction (%)**			**Model Configuration**
		x-direction	y-direction	z-direction	
Un-reinforced	A1-000b	0.0	0.0	0.0	Same as Figure 11 without rebars
Uniaxial	A1-001a/b	0.0	0.0	0.5	Figure 11a
	A1-002	0.0	0.0	1.1	
	A1-003	0.0	0.0	1.5	
Biaxial	A1-101a/b	0.5	0.0	0.5	Figure 11b
	A1-102a/c	0.5	0.0	1.1	
	A1-103	0.5	0.0	1.5	
	A1-202	1.1	0.0	1.1	
	A1-303	1.5	0.0	1.5	
	A3-102-L1	0.5	0.0	1.1	Figure 11d
	A3-202-L2	1.1	0.0	1.1	Figure 11e
	A3-202-L3	1.1	0.0	1.1	Figure 11f
Triaxial	A1-111a/b	0.5	0.5	0.5	Figure 11c
	A1-222	1.1	1.1	1.1	
	A1-211	1.1	0.5	0.5	
	A1-331	1.5	1.5	0.5	
	A1-321a	1.5	1.1	0.5	

Table 3. Properties of the concrete.

Material Property	**Value**
Initial Temperature	10.6 ^{o}C
Initial Relative Humidity	80%
Aggregate Type	Siliceous
Reference Density	2231 kg/m^3
Reference Specific Heat	1100.0 J/(kg K)
Water/Cement Ratio	0.5
Aggregate volume fraction	0.7
Concrete Young's Modulus	37.9 GPa
Rebar Young's Modulus	200 GPa
Concrete Poisson's Ratio	0.22
Rebar Thermal Expansion Coef.	11.3×10^{-6}/K
Rebar Thermal Conductivity	53 W/(m K)
ASR Expansion Char. Time	18.9 days
ASR Expansion Latency Time	18 days
ASR Char. Activation Energy	5400
ASR Latency Activation Energy	9400
ASR Reference Temperature	35 ^{o}C
Activation Temperature for Creep	23 ^{o}C

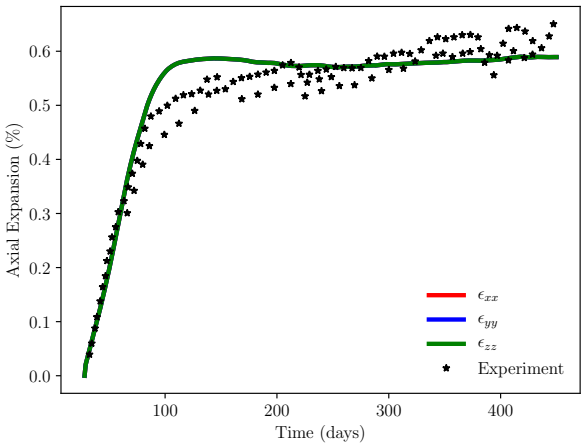

Figure 13. Experimental and simulation results for axial expansion of an unrestrained concrete block (Specimen A1-000b) used for model calibration.

As noted by [9], the start time of the experiment can significantly affect the ASR expansion behavior because of the effects of synchronizing the aging of the concrete with the periods of high temperature, when ASR expansion is accelerated. To illustrate the effect of starting the same experiment at different times of the year, the same unreinforced concrete block was simulated with three different starting times for exposure to the environmental conditions. Here, Set-1 corresponds to the concrete (Specimen A1-000b) expansion as reported by [9] that is used for calibrating the ASR model in BlackBear. Set-2 and Set-3 concretes are considered to have been cast at later times and their testing started approximately from 69 days and 166 days, respectively. Similar dependencies on start time were shown by [9], but for specimens with varying reinforcement configurations, because unreinforced blocks were not actually tested at each of these start times. However, it is advantageous to compare the response of identical unreinforced blocks to highlight the effects of environmental conditions on ASR kinetics. The results of this parameter study shown in Figure 14 clearly demonstrate that starting at a time with a lower temperature impedes the ASR reaction and delays its onset.

The same set of parameters calibrated for the unreinforced block were then applied to predict the expansion of the reinforced concrete block. Figure 15 compares the contours of the local volumetric expansion of the concrete block with no reinforcement (Specimen A1-000b) and with uniaxial reinforcement (Specimen A1-001 from [9]) at the end of the experiment. As can be seen in Figure 15, the presence of rebars constrains the expansion in the axial direction of the bars. It can also be seen that the volumetric expansion is slightly lower along the edges of both blocks, which can be attributed to the relative humidity being lower in the early stages of the experiment because it more closely tracked the environmental conditions. Similar constraining effect is observed for other reinforced concrete cases with varying rebar configurations. The volumetric expansion of the blocks is reduced with the increase in the rebar fraction.

Time histories of the simulated average axial expansion in the three directions are shown compared with experimental results in Figure 16. The constraining effect of the rebar in the z-direction is clearly evident as a decreased expansion in that direction relative to the other two directions. ASR expansion is over-predicted in all directions early in the aging process, but eventually approaches experimental results. This may be due to issues inherent in the ASR expansion or isotropic damage models used here.

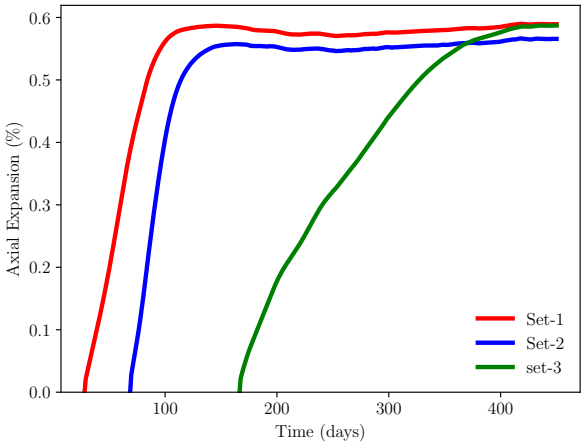

Figure 14. BlackBear simulation results showing the effect of the environmental conditions on the free expansion of a plain concrete block. The start time of exposure of the block to the temperature and relative humidity history shown in Figure 12 is varied to match the times used for the three sets of experiments conducted by [9]. Here, Set-1 corresponds to Specimen A1-000b of [9], but plain concrete specimens were not actually tested in experimental Sets 2 and 3.

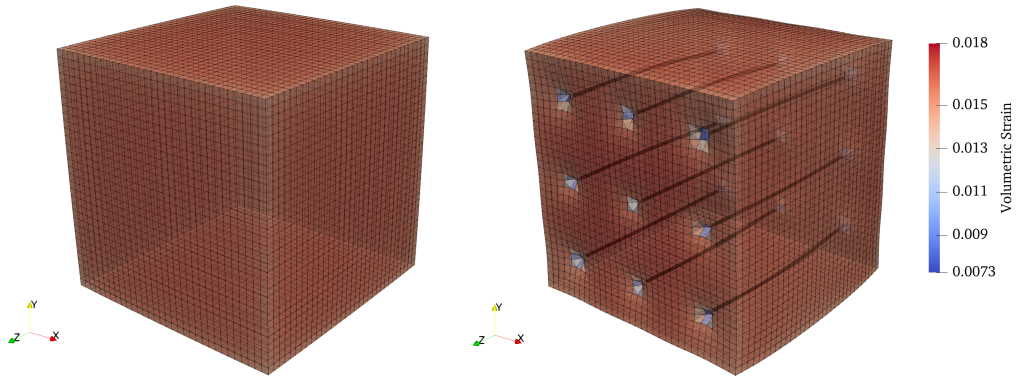

Figure 15. Volumetric expansion of a concrete block with no reinforcement (Specimen A1-000b) (left) and with uniaxial reinforcement (Specimen A1-001a) (right), demonstrating the confinement effect of reinforcement on the overall expansion of the block at the end of the experiment. The deformation is magnified 50× to highlight the confining effect of the bars.

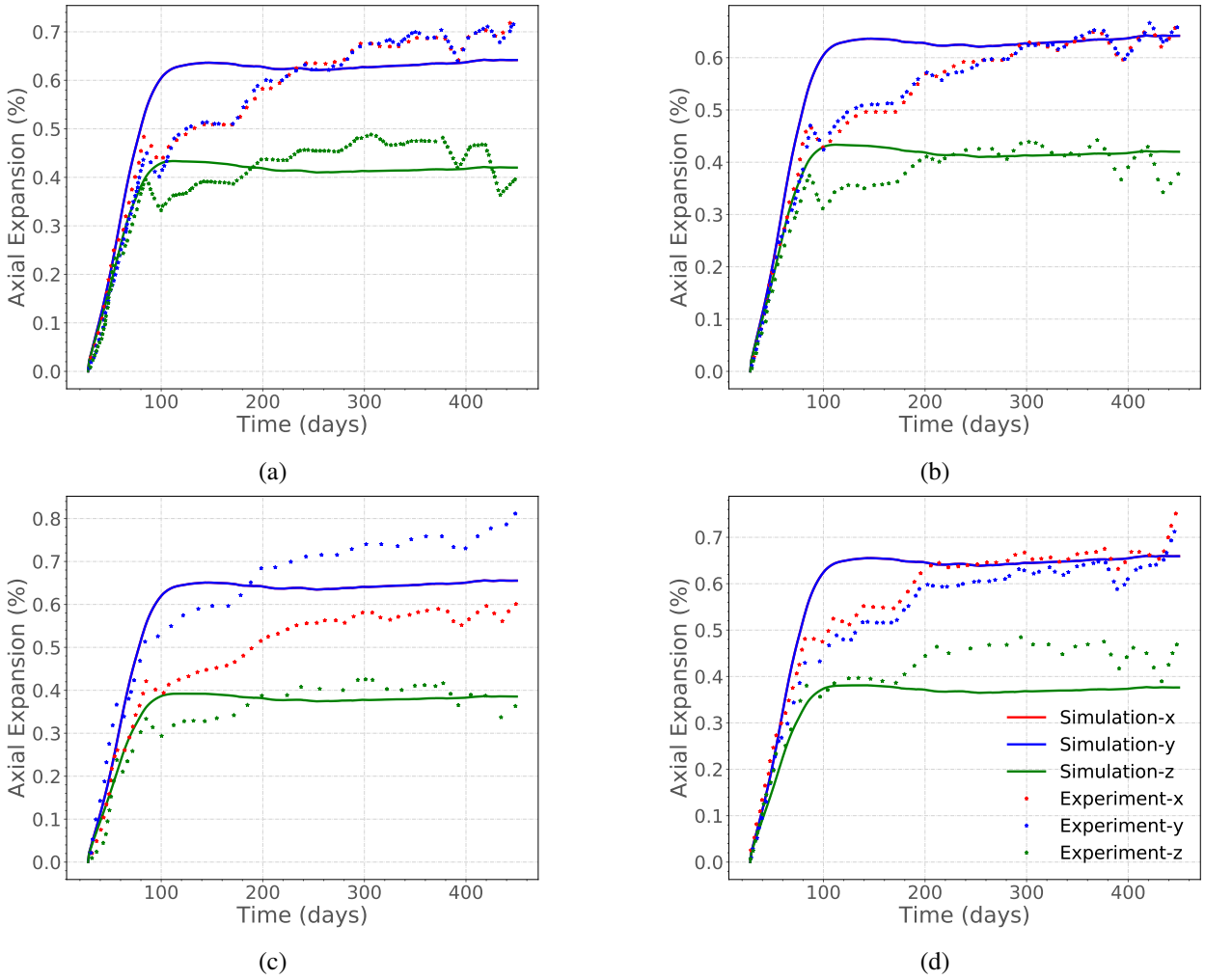

Figure 16. Expansion of uniaxially reinforced concrete specimens (a) A1-001a, (b) A1-001b, (c) A-002, (d) A1-003.

Time histories of the simulated average axial expansion in the three directions for biaxially reinforced concrete block are shown compared with experimental results in Figure 17. The expansion predicted from the simulations most closely matches the experimental behavior for this case. Higher expansion in y-direction indicates less confinement due to lack of rebars in that direction. In addition, the confinement effect varies with the variation of the rebar fraction in the direction obtained by varying the nominal diameter of the rebars.

Time histories of the simulated average axial expansion in the three directions for triaxially reinforced concrete block are shown compared with experimental results in Figure 18. The simulation is over predicting the expansion behavior in almost all the cases here, and needs further investigation. The source of this error is not obvious because the models with biaxially confined concrete reasonably predicted the confining effects in the experiments.

Time histories of the simulated average axial expansion in the three directions for biaxially reinforced concrete block with varying reinforcement configurations are shown compared with experimental results in Figure 19. Although the simulation is over predicting the expansion behavior in all the cases here, it is noteworthy that comparative expansion in each direction predicted from the model follow similar trend as the experimental observations. The casting and experiment of A3 specimens started at later time than the A1 specimens, thus experiencing very different environmental exposure. The experimental study does not

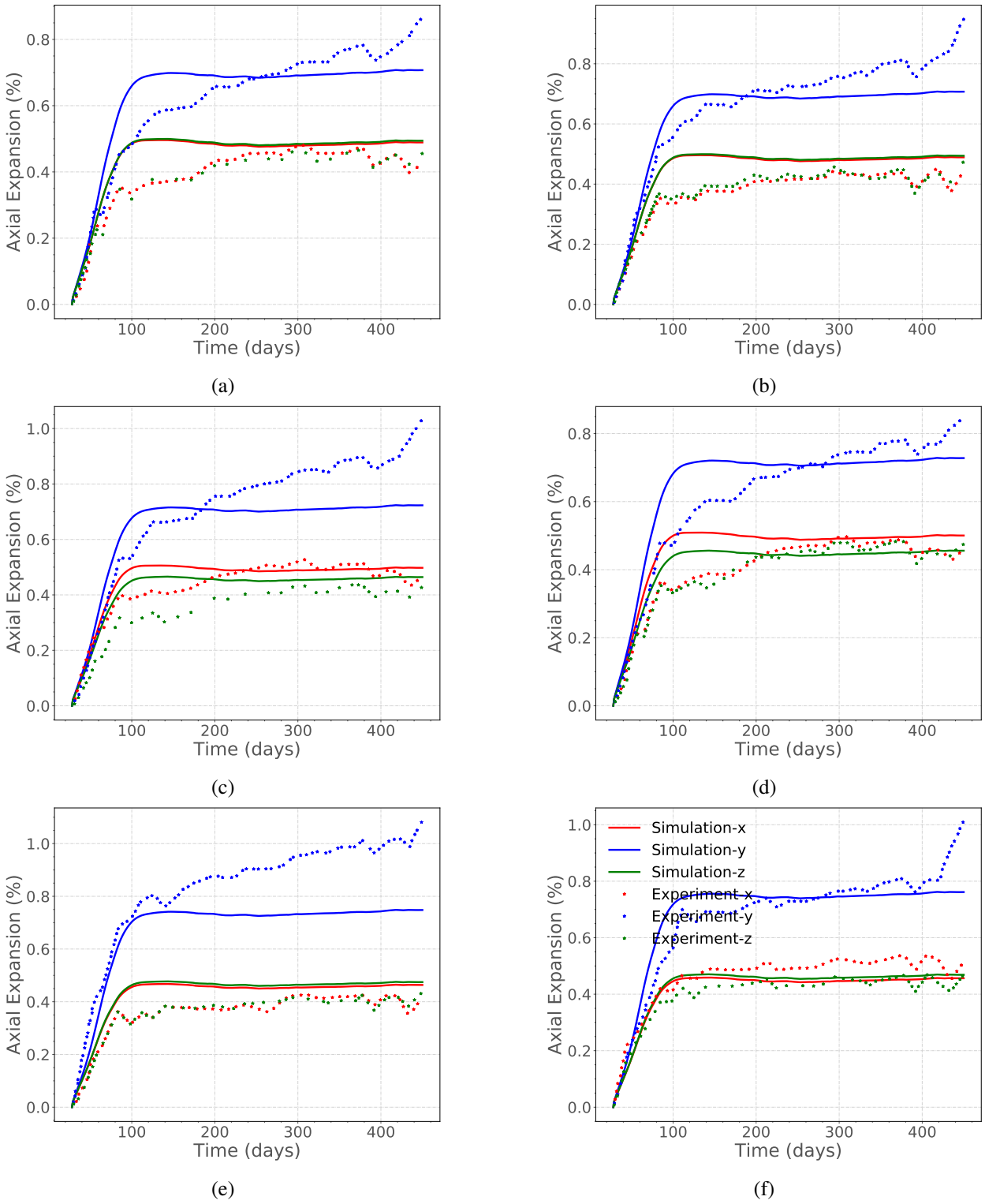

Figure 17. Expansion of biaxially reinforced concrete: (a) A1-101a, (b) A1-101b, (c) A1-102a, (d) A1-103, (e) A1-202, (f) A1-303.

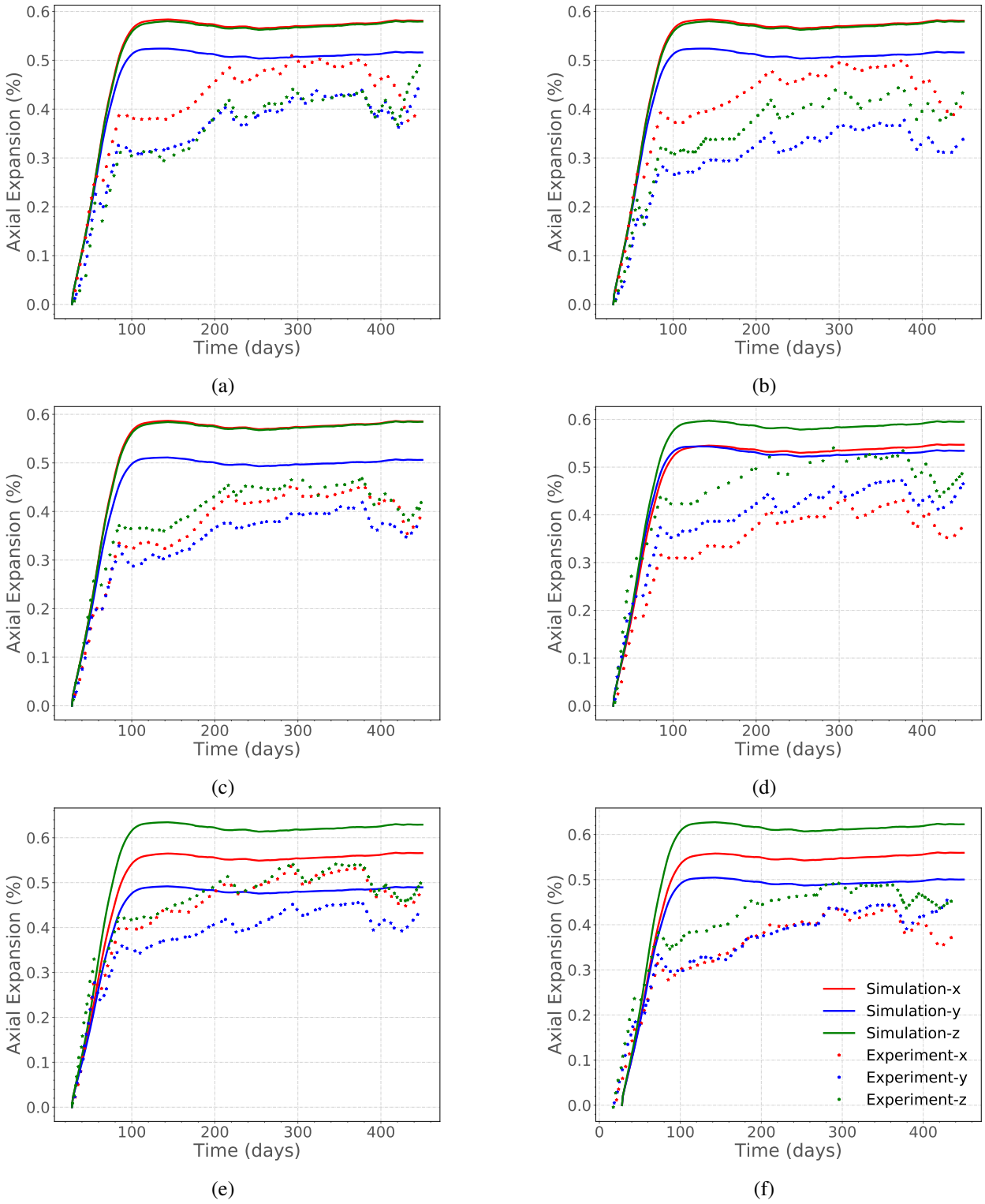

Figure 18. Expansion of triaxially reinforced concrete: (a) A1-111a, (b) A1-111b, (c) A1-222, (d) A1-211, (e) A1-331, (f) A1-321a.

provide any information about how a plain concrete block from this set of specimens expand. Due to lack of information, the ASR model calibrated with respect to the behavior of the A1 specimens has been used here. More fine tuning of the model (specifically reducing the maximum expansion value) is necessary to appropriately capture the expansion behavior from this set of experiments.

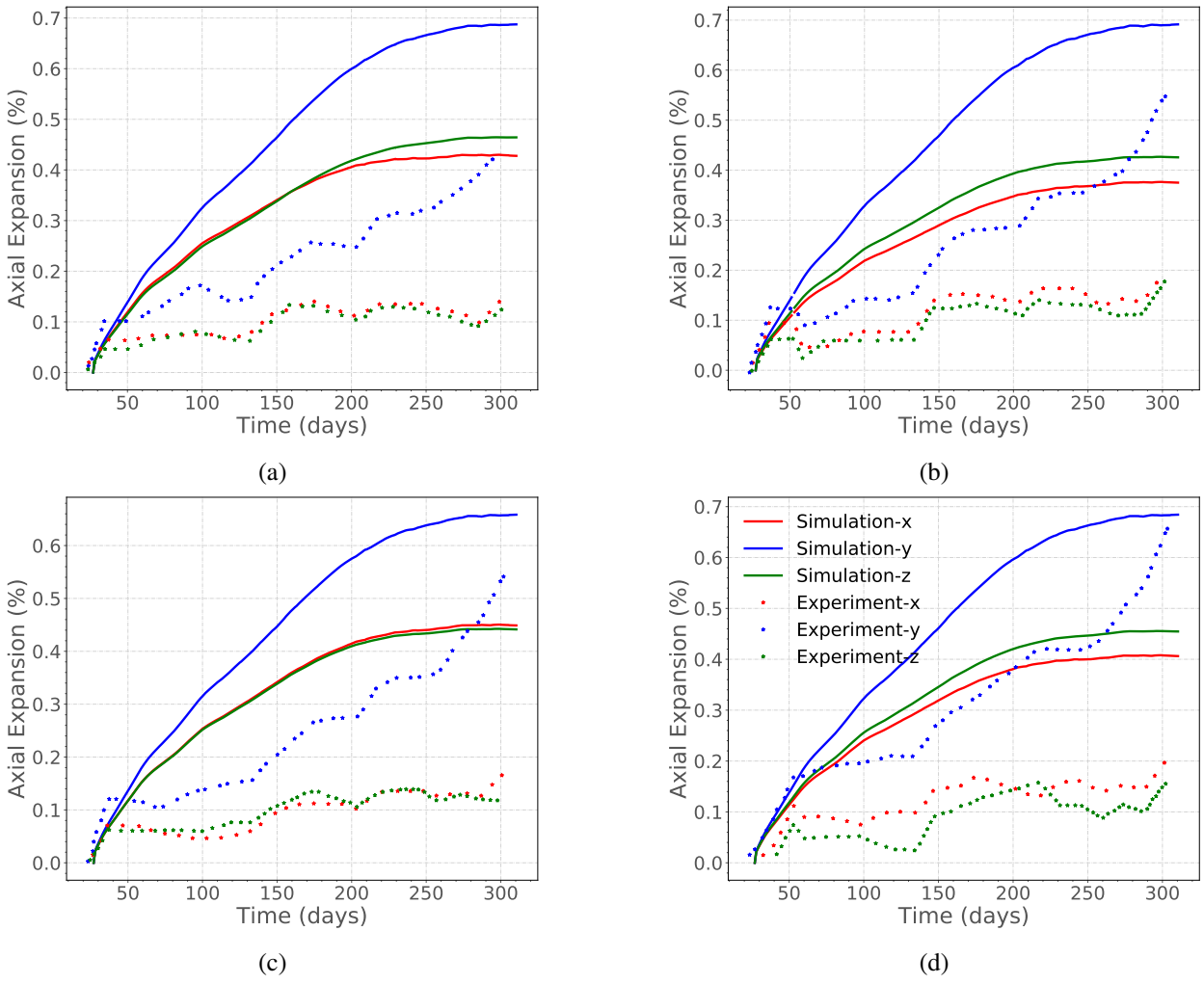

Figure 19. Axial expansion with variable biaxial reinforcement layout: (a) A3-102c, (b) A3-102-L1, (c) A3-202-L2, (d) A3-202-L3.

Here we presented a preliminary set of cases built to evaluate and validate the multiphysics modeling capability of BlackBear. The primary focus this year has been to examine the free expansion of concrete blocks and beams due to ASR. Confinement effect due to presence of reinforcement bars has been observed. For most of the cases, when the model is calibrated for similar environmental conditions as the experiments, model predictions closely match the experimental observations, specifically in the early stage. However, the model follows the expansion behavior proposed by Larive [11] which flattens out quickly after the onset of ASR. Wallau et. al. [12] has shown that the ASR expansion model proposed by Mukhopadhyay and Liu [13] shows better compliance with their experimental data. Such additional models needs to be implemented in BlackBear to expand its modeling capabilities. Furthermore, in the future, more validation cases will be built to validate other degradation mechanisms of concrete and enhance the problem suite with large structural models.

4.2 Reinforced Concrete Beam Member

This section considers numerical modeling of a biaxially reinforced concrete (RC) beam member which was subjected to ASR expansion by Wald [14], as shown in Figure 20. Reactive cement and aggregate were used in the mix proportion, as indicated in Table 4, to accelerated the ASR expansion in the beam. The RC member was divided into three zones as indicated in Figure 21 to study the ASR swelling in different environmental conditions and reinforcement confinement. The environmental conditions (temperature and relative humidity) and reinforcement confinement in three zones are shown in Figure 21. Zones A and B were subjected to a periodically moist conditions at temperature as shown in Figure 22, while Zone C was subjected to a constant wet conditioning at 5°C–10°C more than the seasonal temperature in Zones A and B. The relative humidity conditions in Zones A and B are shown in Figure 23, while in Zone C, it was in between 90% and 100%. Zone A corresponds to the part of the beam which has no confinement reinforcement in the Z direction, while Zones B and C correspond to the part of the beam which has confined reinforcement in both Y and Z directions. ASR expansion was monitored separately in each zone to using calipers and vibrating wire gages; however, the only measurement from caliper was used in this study as Wald [14] reported that vibrating wire gage measurements were used only for validation and comparison. The measurement from caliper provides four expansion measurement along x and y directions and two measurements along the z-direction.

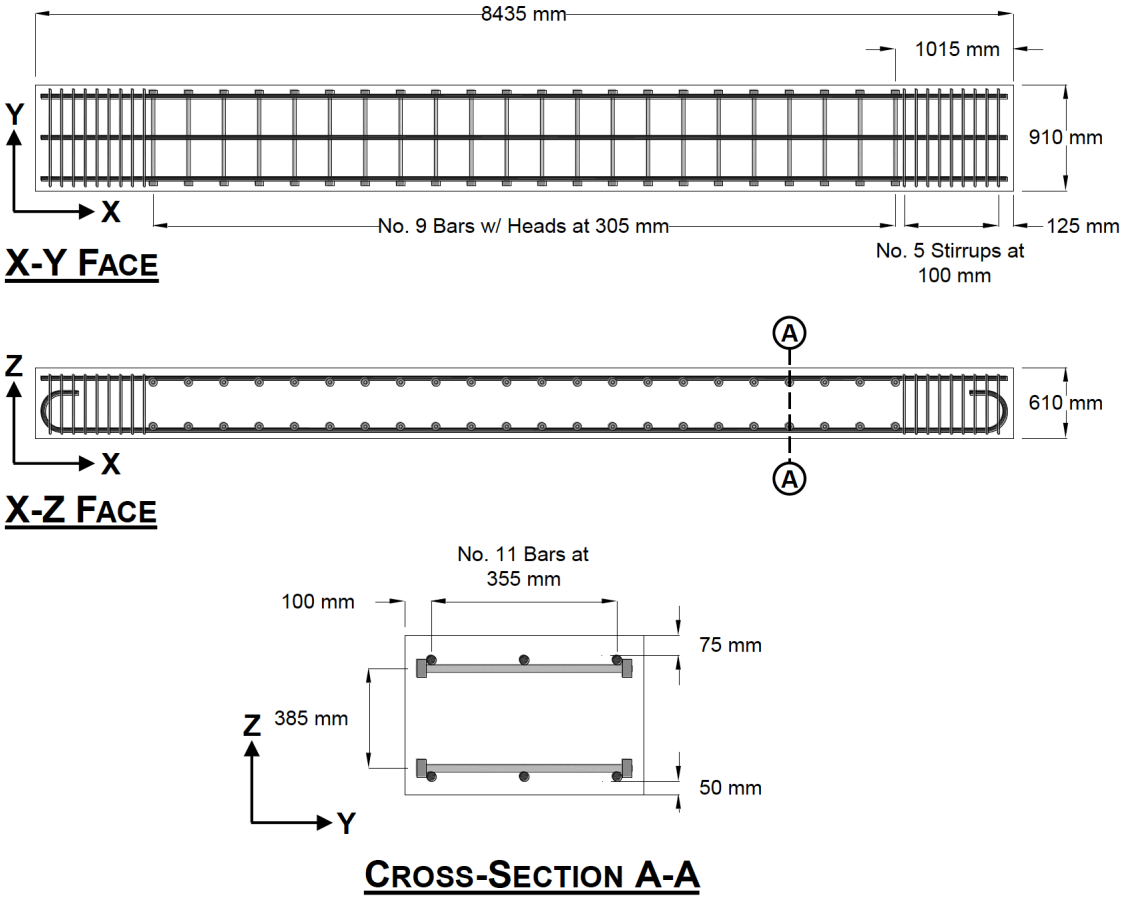

Figure 20. Biaxially RC beam member.

Table 4. Mix proportion of concrete and properties of RC beam.

Material/Parameter	**Properties/Quantity**
Concrete	highly reactive concrete mix
Cement	high alkali type I/II with 1.1% alkali content
Coarse Aggregate	50-50% blend of low and high reactive 19 mm crushed coarse aggregate containing quartz and granite
Fine Aggregate	highly reactive concrete sand containing quartz, chert, and feldspar
NaOH	50% NaOH was added to the mixing water to boost equivalent alkali content to 1.25%
Reinforcement	ASTM A615 grade 60
water-cement ratio	0.5
$f_c^{'}$ at 28 days	33 MPa (measured value) 31 MPa (designed value)

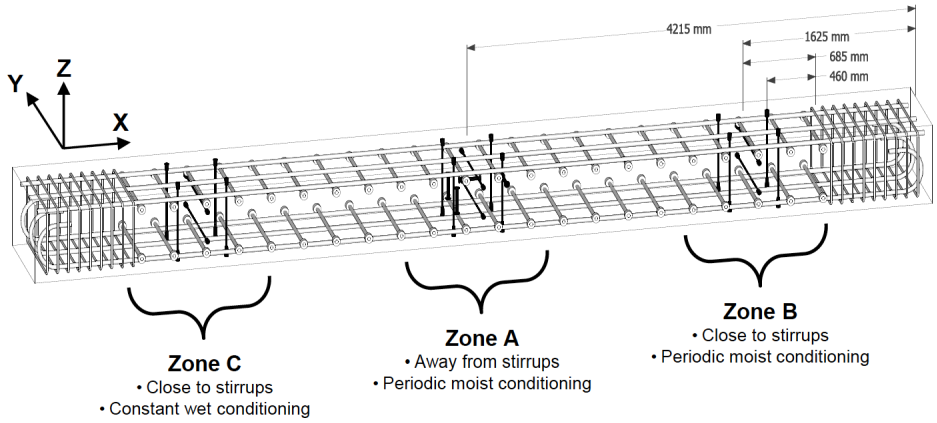

Figure 21. Three zones in the RC beam member.

The BlackBear finite element model of this beam is shown in Figure 24. The modeling parameters for the beam are indicated in Table 5. The FE RC beam model is divided into three blocks corresponding to Zones A, B, and C in the experiment. Zones A and B are subjected to the same temperature and relative humidity boundary conditions as observed during the exposure period in the experiment (as shown in Figures 22–23). Zone C is subjected to 95% relative humidity boundary conditions and temperature boundary conditions that are the same as those in Zones A and B (the authors are in process of applying boundary conditions as observed in experiment, which is 5°C-10°C more than temperature observed in Zones A and B). ASR expansion from the simulation in Zones A, B, and C in the X, Y, and Z directions are compared with that from the experimental results from [14] in Figure 25. The simulations predict the ASR expansion along each direction reasonably well until the latency period, (i.e., 60 days). Beyond the latency period, simulations overpredict the ASR expansion in the X and Y directions as compared to the results from experimental study. In the Z direction, ASR expansion from the simulation could not increase as fast as observed in the experiment. Differences in the confinement reinforcement along Y and Z directions cause the differences in the ASR expansion in these two zones Furthermore, simulation captures the effect of differences in the environmental boundary conditions on ASR expansion in Zones B and C. Moreover, it is observed that along

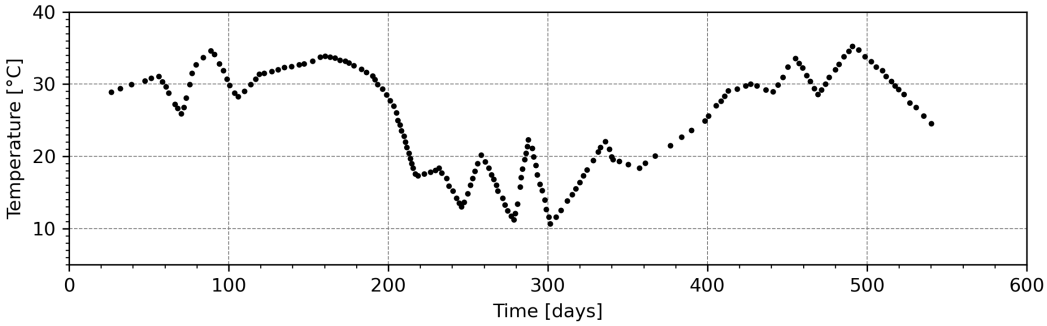

Figure 22. Temperature history during the exposure period.

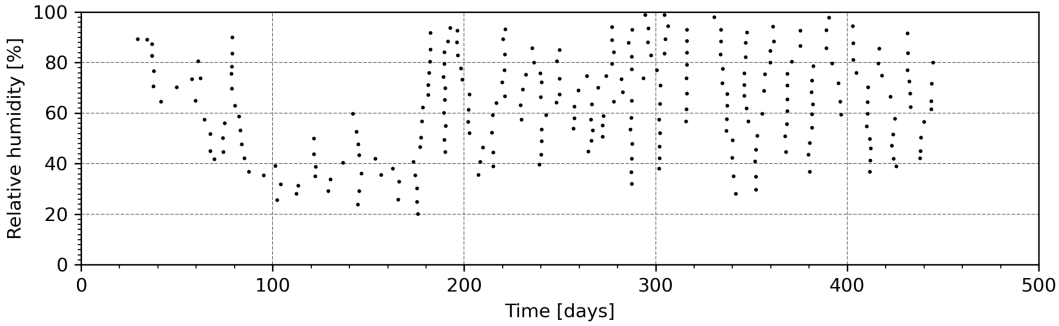

Figure 23. Relative humidity history during the exposure period.

the X and Y directions, the differences in reinforcement confinement and environmental boundary conditions does not affect the ASR expansion in these directions, which is aligned with finding of the experimental study. Additionally, results for volumetric strain from the simulation are compared with experimental results in Figure 26. Similar to the ASR expansion, the simulation follows the experimental until the latency period. However, beyond the latency period, the simulation could not follow the experimental trend.

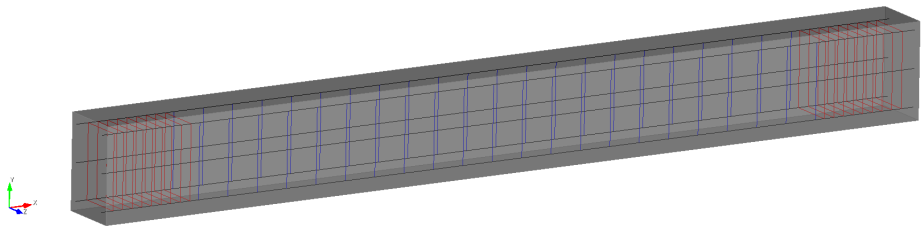

Figure 24. Biaxial RC beam model in BlackBear.

4.3 Concrete Modeling Summary

BlackBear simulations were performed here on two sets of experiments by the same group on concrete blocks and beams subjected to accelerated ASR. These experiments tested a number of capabilities of BlackBear for modeling concrete, including the ASR and creep models and the models for reinforcement.

Table 5. Modeling parameters used in BlackBear.

Parameter	**Value**
Aggregate type	Siliceous
Aggregate pore type	dense
Aggregate mass	1877.0 kg/m^3
Cement type	US type 1
Cement mass	354.0 kg/m^3
Water-cement ratio	0.5
Concrete cure time	28.0 days
Aggregate volume fraction	0.7
Reference density of concrete	2231.0 kg/m^3
Poisson's ratio	0.22
Young's modulus	37.3×10^9 N/m^2
Recoverable Young's modulus	37.3×10^9 N/m^2
Residual Young's modulus fraction	0.1
Recoverable viscosity	1
Long term viscosity	1
Long term characteristic time	1
Compressive strength	33.0×10^6 N/m^2
Compressive stress exponent	0.0
Expansion stress limit	8.0×10^6 N/m^2
Tensile strength	3.2×10^6 N/m^2
Tensile retention factor	1.0
Tensile absorption factor	1.0
Residual tensile strength fraction	1.0
Activation temperature	23.0°C
Reference temperature for ASR expansion	35.0°C
Max volumetric expansion	0.031
Characteristic time	25 days
Latency time	60 days
characteristic activation energy	5400.0
latency activation energy	9400.0
Stress latency factor	1.0
Relative humidity exponent for ASR volumetric strain	1.0
Moisture diffusivity model	Bazant
Coupled moisture diffusivity factor	1.0e-2
Thermal conductivity model	Kodur-2004
Thermal capacity model	Kodur-2004
Reference specific heat of concrete	1100.0 J/(Kg K)
Reference thermal conductivity of concrete	3 W/(m K)
Concrete thermal expansion coefficient	8.0×10^{-6} 1/°C
Steel thermal expansion coefficient	11.3×10^{-6} /K
Stress free temperature	10.6 °C

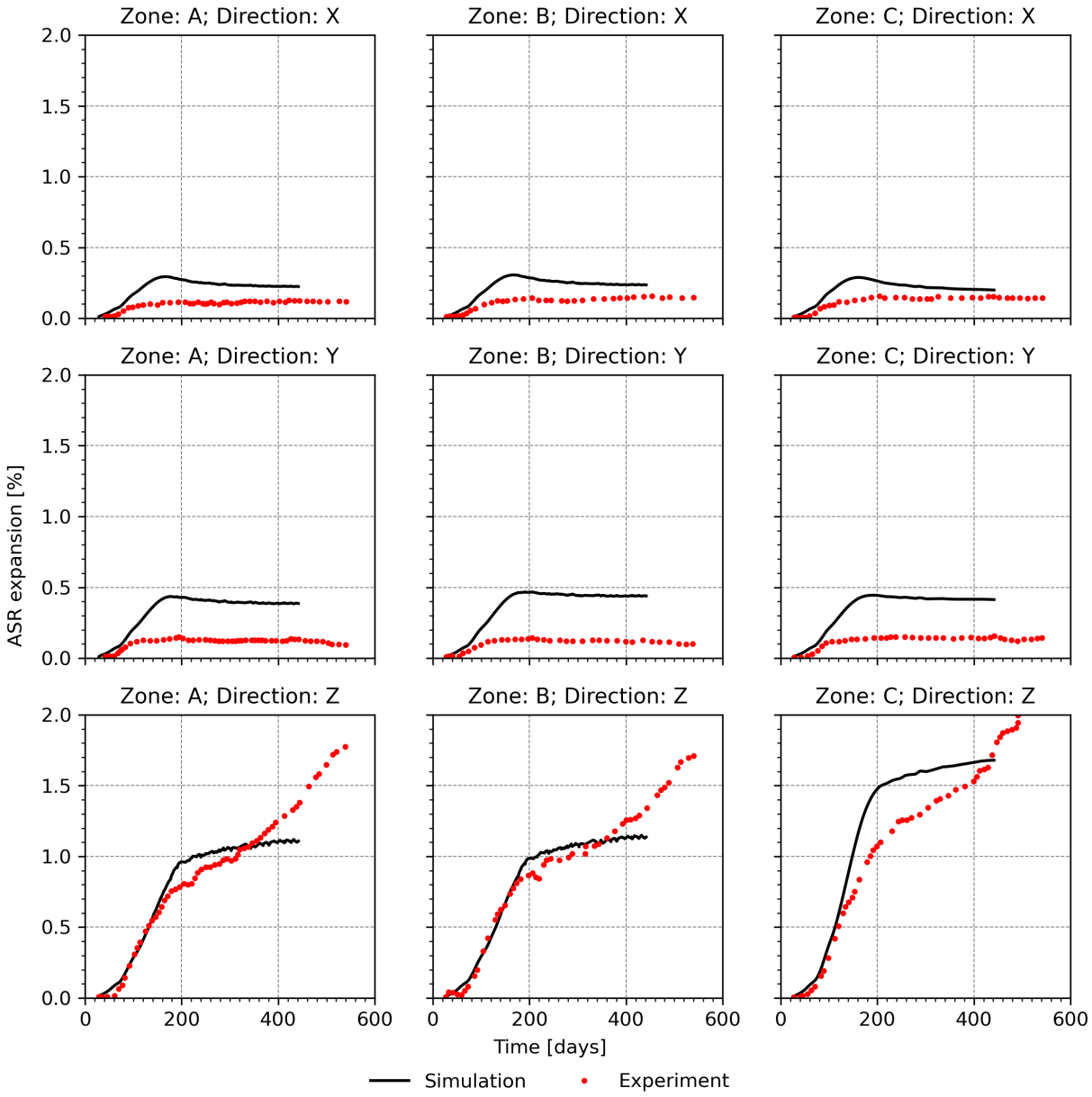

Figure 25. ASR expansion in Zones A, B, and C along X, Y, and Z directions.

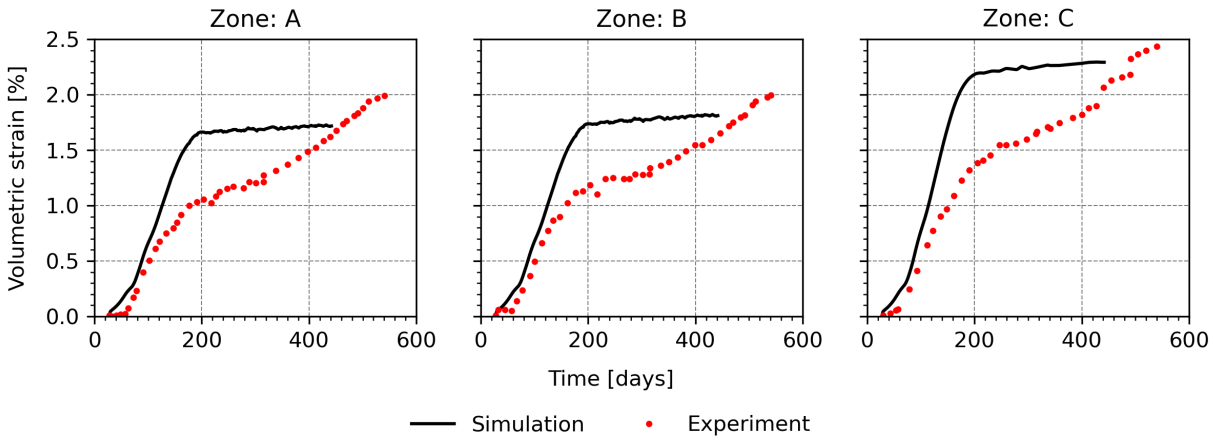

Figure 26. Volumetric strain in Zones A, B, and C.

In general, the results are quite encouraging. The models capture the important phenomena, and in most cases accurately capture the confining effects of rebar. For both the concrete prisms and the beam, the models underrepresent the effect of confining under triaxial confinement, which warrants further investigation. Also, for both sets of experiments, the ASR model used here tends to predict excessive expansion early on, but the expansion then reaches a plateau in the expansion and underpredicts the expansion. Other ASR expansion models should be investigated to see if they provide more realistic response.

Multiple other studies are available, and this set of validation cases should be expanded to include a broader set of experimental data from other sources and for other structural configurations.

5 Summary

The integrity of RPVs and reinforced concrete structures are critical for the long-term operation of existing LWR nuclear power plants. As demonstrated in this report, foundational capabilities for analysis of both types of these structures are reaching a level of maturity that allows them to begin to be applied to engineering problems of interest to evaluate their applicability.

Extensive testing is required to develop confidence in a code applied to such applications, and this report documents initial testing of the following capabilities:

- **PFM analysis of RPV integrity:** Grizzly's PFM models evaluate random realizations of plausible populations of flaws present in an RPV to compute the probability of fracture initiation. These models use the thermo-mechanical response of the RPV under a given transient loading scenario as input. Prior work has benchmarked the models of the thermo-mechanical response as well as the deterministic fracture models used as part of the PFM calculations. The analyses here systematically compared PFM solutions from Grizzly against benchmark solutions for individual regions of an RPV, as well as multiple representative RPV configurations.
  In general, these comparisons were favorable, although there are some specific cases with significant enough deviations from the reference configurations to warrant further study. Further work is also needed to improve the model for initiation, growth, and arrest for better comparison with reference solutions. This set of models should also be expanded to test more combinations of modeling features.
  This benchmarking exercise is important to establish that the baseline capability is a faithful implementation of the models on which it was based. Once this is established, advanced features, such as the multidimensional capabilities of Grizzly, can be used for more realistic simulations of aspects of the RPV integrity problem that have previously not been possible. A proof-of-concept simulation of a cold plume effect was demonstrated as an example of one such application.

- **ASR expansion models for concrete structures:** Recent developments in Grizzly and BlackBear have allowed them to model the major phenomena in reinforced concrete degradation, including models for thermal, moisture, and chemical species transport, ASR and RIVE, creep and damage, and reinforcing bars and their interactions with the concrete matrix. Because of its importance for present issues in LWRs, as well as the available experimental data, ASR was chosen as an initial degradation mechanism for validation testing. A series of experiments on concrete specimens subjected to accelerated ASR were simulated in BlackBear. These included concrete prisms with varying amounts of reinforcement as well as a concrete beam.
  Comparisons with experimental data were generally good and captured important phenomena such as the effects of confinement in some cases, although there are some areas that indicate needs for further model refinement. The models overpredicted the expansion in cases with triaxial confinement and could use improvement in the way the history of ASR expansion is represented. Future work should evaluate other ASR models or modifications to the existing models to see if they offer improved predictions. In addition, similar testing is needed for the models of RIVE and other degradation mechanisms.

This work represents important and necessary progress in the development of Grizzly and BlackBear. However, it is important to emphasize that this testing is by no means complete and further testing on similar problems, as well as on more representative structures of increasing complexity, is important to develop confidence in the predictive capabilities of these codes.

6 References

[1] R. K. Nanstad, T. M. Rosseel, M. A. Sokolov, W. L. Server, T. Arai, N. Soneda, R. Dyle, G. R. Odette, M. T. Kirk, B. N. Burgos, and B. J. Hall. *Expanded Materials Degradation Assessment (EMDA) Volume 3: Aging of Reactor Pressure Vessels*. Tech. rep. NUREG/CR-7153, Vol. 3, ORNL/TM-2013/532. Oak Ridge, TN: Oak Ridge National Laboratory, Oct. 2014.

[2] H. Graves, Y. Le Pape, D. Naus, J. Rashid, V. Saouma, A. Sheikh, and J. Wall. *Expanded Materials Degradation Assessment (EMDA) Volume 4: Aging of Concrete and Civil Structures*. Tech. rep. NUREG/CR-7153, Vol. 4, ORNL/TM-2013/532. Oak Ridge, TN: Oak Ridge National Laboratory, Oct. 2014.

[3] B. W. Spencer, W. M. Hoffman, D. Schwen, and S. Biswas. *Progress on Grizzly Development for Reactor Pressure Vessels and Reinforced Concrete Structures*. Tech. rep. INL/EXT-19-56012. Idaho National Laboratory, Sept. 2019.

[4] *BISON Users Manual, BISON Release 1.5*. Tech. rep. INL/MIS-18-50577 Rev. 001. Idaho National Laboratory, 2018.

[5] B. Spencer, W. Hoffman, and M. Backman. "Modular system for probabilistic fracture mechanics analysis of embrittled reactor pressure vessels in the Grizzly code". In: *Nuclear Engineering and Design* 341 (Jan. 2019), pp. 25–37.

[6] T. Dickson, P. T. Williams, B. R. Bass, and H. B. Klasky. *Fracture Analysis of Vessels – Oak Ridge, FAVOR, v16.1, Computer Code: User's Guide*. Tech. rep. ORNL/LTR-2016/310. Oak Ridge, TN: Oak Ridge National Laboratory, Sept. 2016.

[7] G. J. Schuster, S. R. Doctor, A. F. Pardini, and S. L. Crawford. *Characterization of Flaws in U.S. Reactor Pressure Vessels*. Tech. rep. NUREG/CR-6741, Vol. 2, PNNL-11143B. Richland, WA: Pacific Northwest National Laboratory, Aug. 2000.

[8] P. Williams, T. Dickson, B. R. Bass, and H. B. Klasky. *Fracture Analysis of Vessels – Oak Ridge, FAVOR, v16.1, Computer Code: Theory and Implementation of Algorithms, Methods, and Correlations*. Tech. rep. ORNL/LTR-2016/309. Oak Ridge, TN: Oak Ridge National Laboratory, Sept. 2016.

[9] D. M. Wald, M. T. Allford, O. Bayrak, and T. D. Hrynyk. "Development and multiaxial distribution of expansions in reinforced concrete elements affected by alkali–silica reaction". In: *Structural Concrete* 18 (2017), pp. 914–928.

[10] B. W. Spencer, W. M. Hoffman, S. Biswas, W. Jiang, A. Giorla, and M. A. Backman. "Grizzly and BlackBear: Structural Component Aging Simulation Codes". In: (in review).

[11] C. Larive. "Apports Combin'es de l'Experimentation et de la Modélisation à la Comprehension del' A lcali-Réaction et de ses Effets Mécaniques," PhD thesis. Laboratoire Central des Ponts et Chaussées, Paris., 1998.

[12] W. Wallau, S. Pirskawetz, K. Voland, and B. Meng. "Continuous expansion measurement in accelerated concrete prism testing verifying ASR-expansion models". In: *Materials and Structures* 51.79 (2018).

[13] K. W. Liu and A. K. Mukhopadhyay. "A kinetic-based ASR aggregate classification system". In: *Constr Build Mater* 68.525 (2014).

[14] D. M. Wald. "ASR expansion behavior in reinforced concrete: experimentation and numerical modeling for practical application". PhD thesis. 2017.